Charged particle decay of hot and rotating ^{88}Mo nuclei in fusion-evaporation reactions

S. Valdré,[1,2,*] S. Piantelli,[2] G. Casini,[2] S. Barlini,[1,2] S. Carboni,[1,2] M. Ciemała,[3] M. Kmiecik,[3] A. Maj,[3] K. Mazurek,[3] M. Cinausero,[4] F. Gramegna,[4] V. L. Kravchuk,[5] L. Morelli,[6] T. Marchi,[4] G. Baiocco,[7] L. Bardelli,[1,2] P. Bednarczyk,[3] G. Benzoni,[8] M. Bini,[1,2] N. Blasi,[8] A. Bracco,[8,9] S. Brambilla,[8] M. Bruno,[6] F. Camera,[8,9] A. Chbihi,[10] A. Corsi,[8,9] F. C. L. Crespi,[8,9] M. D'Agostino,[6] M. Degerlier,[11] D. Fabris,[12] B. Fornal,[3] A. Giaz,[8,9] M. Krzysiek,[3] S. Leoni,[8,9] M. Matejska-Minda,[3,13] I. Mazumdar,[14] W. Męczyński,[3] B. Million,[8] D. Montanari,[8,9] S. Myalski,[3] R. Nicolini,[8,9] A. Olmi,[2] G. Pasquali,[1,2] G. Prete,[4] O. J. Roberts,[15] J. Styczeń,[3] B. Szpak,[3] B. Wasilewska,[3] O. Wieland,[8] J. P. Wieleczko,[10] and M. Ziębliński[3]

[1]*Dipartimento di Fisica, Università di Firenze, I-50019 Sesto Fiorentino, Italy*
[2]*INFN sezione di Firenze, I-50019 Sesto Fiorentino, Italy*
[3]*Institute of Nuclear Physics Polish Academy of Sciences, 31-342 Kraków, Poland*
[4]*INFN, Laboratori Nazionali di Legnaro, I-35020 Legnaro, Italy*
[5]*National Research Centre "Kurchatov Institute", 123182 Moscow, Russia*
[6]*Dipartimento di Fisica e Astronomia, Università di Bologna and INFN sezione di Bologna, I-40127 Bologna, Italy*
[7]*Dipartimento di Fisica, Università di Pavia, Italy and INFN sezione di Pavia, I-27100 Pavia, Italy*
[8]*INFN sezione di Milano, I-20133 Milano, Italy*
[9]*Dipartimento di Fisica, Università di Milano, I-20133 Milano, Italy*
[10]*Grand Accélérateur National d'Ions Lourds (GANIL), BP 55027, F-14076 Caen Cedex 5, France*
[11]*Nevsehir Haci Bektas Veli University, Science and Art Faculty, Physics Department, TR-50300 Nevsehir, Turkey*
[12]*INFN, Sezione di Padova, I-35131 Padova, Italy*
[13]*Heavy Ion Laboratory, University of Warsaw, 02-093 Warsaw, Poland*
[14]*Tata Institute of Fundamental Research, 400005 Mumbai, India*
[15]*University of York, Heslington, YO10 5DD York, United Kingdom*

(Received 11 September 2015; published 21 March 2016)

A study of fusion-evaporation and (partly) fusion-fission channels for the ^{88}Mo compound nucleus, produced at different excitation energies in the reaction ^{48}Ti + ^{40}Ca at 300, 450, and 600 MeV beam energies, is presented. Fusion-evaporation and fusion-fission cross sections have been extracted and compared with the existing systematics. Experimental data concerning light charged particles have been compared with the prediction of the statistical model in its implementation in the GEMINI++ code, well suited even for high spin systems, in order to tune the main model parameters in a mass region not abundantly covered by exclusive experimental data. Multiplicities for light charged particles emitted in fusion evaporation events are also presented. Some discrepancies with respect to the prediction of the statistical model have been found for forward emitted α particles; they may be due both to pre-equilibrium emission and to reaction channels (such as deep inelastic collisions or quasifission/quasifusion) different from the compound nucleus formation.

DOI: 10.1103/PhysRevC.93.034617

I. INTRODUCTION

The study of the de-excitation of compound nuclei (CN) dates back to the beginning of modern nuclear physics, but it has found renewed interest in recent years (see, for example, [1] for medium mass systems and [2–5] for very light systems) thanks to the improvement of experimental techniques, allowing for a cleaner selection of exclusive decay channels. In this way it is possible to put stringent constraints on the ingredients of the statistical model, commonly used to describe the decay of a compound nucleus at excitation energies below 3 MeV/nucleon. The hypothesis behind the use of this model is that compound nuclei are equilibrated systems, whose decay is independent of their previous history (i.e., the way in which they were formed), but depends on the statistical competition among all the open channels. The decay width of each channel depends on the phase space available in the final state and on the amplitude of the transition matrix. The tuning of the parameters of the statistical model on the basis of the experimental data obtained from compound nucleus reactions is important not only for the topic of low energy fusion reactions, but also for other classes of nuclear processes. In fact many kinds of reactions, from low (5–10 MeV/nucleon) to high ($\gtrsim$100 MeV/nucleon) beam energies, such as deep inelastic collisions, multifragmentation, spallation, etc., can be theoretically described by means of models of the interaction phase [e.g., dynamical models such as Boltzmann Nordheim Vlasov (BNV) [6], antisymmetrized molecular dynamics (AMD) [7], etc.] followed by a statistical "afterburner" for the hot products. Since in many cases the effects related to the nuclear interaction phase under investigation are weak and blurred by secondary decay, it is important to describe the statistical decay as well as possible in order to reduce the uncertainties on the dynamical stage. A good control of the decay process is also mandatory in GDR (giant dipole

*valdre@fi.infn.it

 ©2016 American Physical Society

resonance) or DDR (dynamical dipole resonance) studies because the collective excitation features are extracted from continuous spectra dominated by the statistical γ rays from the source, which must be therefore correctly described by models.

The present work deals with the investigation of fusion-evaporation and fusion-fission channels for the ^{88}Mo compound nucleus at three different excitation energies, produced in the reaction $^{48}\mathrm{Ti} + {}^{40}\mathrm{Ca}$ at 300, 450, and 600 MeV beam energy. In particular, we compared the experimental energy spectra and multiplicities of light charged particles with the prediction of GEMINI++ code [8], a widely used implementation of the statistical model, in order to constrain the relevant parameters in a mass-energy-spin region in which not many experimental data of exclusive type, with a clean selection of the fusion channel, are available. Moreover, in this work we have also extracted the experimental cross sections for the fusion-evaporation and the fusion-fission channels, obtaining values compatible with the existing systematics [9].

This experiment is part of a measurement campaign aimed at the investigation of hot, rotating ^{88}Mo nucleus. The results concerning GDR γ decay are presented in [10,11]. The ^{88}Mo nucleus, like other medium mass nuclei, is a good candidate for this kind of study because it presents a significant fission barrier even at high rotational energy, and it consequently has low fission probability also at high spin values [12]. The use of GEMINI++ as statistical code to be compared with our experimental data is thus a good choice, since this code is particularly well suited for the decay of high spin nuclei.

Among the data available in literature for the mass region $A < 100$ we can cite, for example, [13], where the inclusive decay of ^{67}Ga at 91 MeV excitation energy has been investigated. Proton and α-particle spectra at some polar angles have been compared with the prediction of a statistical code; a good agreement for α-particle center-of-mass energy spectra is obtained if a deformation of the source is taken into account. In contrast, proton energy spectra are not well reproduced. Instead, the angular distributions fit quite well with the prediction of the code for both protons and α particles, when a deformed source is used.

An inclusive study of two different reactions producing the same compound nucleus ^{67}Ga at 1.9 MeV/nucleon excitation energy is presented in [14]. The authors found that it is not possible to describe both the energy spectra and the angular distributions of α particles by means of a statistical code with a unique set of parameters; moreover, proton energy spectra require reduced evaporation barriers to be well reproduced.

In [15] proton and α energy spectra in coincidence with evaporation residues have been measured for the reaction $^{32}\mathrm{S} + {}^{74}\mathrm{Ge}$ at different beam energies in the range 5–13 MeV/nucleon. From the comparison with statistical model predictions, the reverse level density parameter $K = \frac{A}{a}$ is found to be substantially independent of the excitation energy of the system in the mass region around $A = 100$. The dependence of K on the angular momentum has been investigated in [1] for the compound nuclei ^{97}Tc and ^{62}Zn at 36 MeV excitation energy, comparing the energy spectra of neutrons, protons, and α particles with the prediction of the CACARIZO code (a Monte Carlo version of the CASCADE statistical model code [16]); the angular momentum selection was performed by means of the γ multiplicity. The authors found that the deformation of the source (taken into account by means of the deformability parameters included in the code) has no effect on neutron and proton energy spectra, while it significantly modifies those of α particles for the lighter compound nucleus. The K values extracted from proton, neutron, and α-particle spectra are different, but they all show a decrease when the angular momentum of the source increases (in the range 13–22 $\hbar$).

In [17] α energy spectra detected in coincidence with evaporation residues (ER) from ^{56}Ni CN produced in the symmetric reaction $^{28}\mathrm{Si} + {}^{28}\mathrm{Si}$ at 112 MeV beam energy are compared with the prediction of CACARIZO. The experimental energy spectra have been well reproduced by introducing a high degree of deformation (corresponding to a quadrupole deformation parameter equal to 0.5) which modifies the effective moment of inertia of nuclei, thus lowering the yrast line. In this way the decay chain becomes longer and α particles are emitted later in the cascade, with smaller average kinetic energy. The authors claimed also that deformation at high spin values is particularly favored if the entrance channel is mass symmetric. Note that the spin range explored by this system is lower than in the present ^{88}Mo case; in fact the critical angular momentum for fusion was $34\hbar$ in [17], while it is $64\hbar$ in our case.

In [18] a detailed study of the transmission coefficients of the statistical model, based on the energy spectra of hydrogen isotopes and α particles evaporated by compound nuclei of ^{96}Ru at 1.2 MeV/nucleon excitation energy, is presented. α-particle spectra are found to be in good agreement with the prediction of the statistical model (CASCADE code) if reduced barriers with respect to the prescription of the optical model are used. Moreover, the level density has to be enhanced, indicating the onset of deformations at high spins (kept into account by lowering the yrast line as done in [17]). For protons, in contrast, the authors explain the unsatisfactory agreement between experimental and simulated energy spectra with the need of taking into account dynamical effects.

In [19] and [20] spectra of α particles emitted from ^{46}Ti CN with 85 MeV excitation energy and critical angular momentum of $35\hbar$ are discussed and compared with the prediction of the already cited CACARIZO code. Various parametrizations of the yrast line implying different degrees of deformation of the CN have been tested, obtaining reasonable agreement with the experimental data. In particular, energy spectra of α particles detected in coincidence with a residue of $Z = 20$ (corresponding to chains in which only one α particle is emitted) can be reproduced only if an extremely high value of the deformation parameter is used. The authors interpret this fact as due either to the presence of a dynamical hyperdeformed state or to the pre-equilibrium emission from a dinuclear system not completely fused. This study is coupled to the investigation of the GDR, confirming the presence of a strongly deformed structure.

In summary, all these studies demonstrate that the decay features of light systems with high spin (up to $\sim 60\hbar$) are a difficult task for available statistical codes. In fact, a single parametrization is often not able to reproduce both proton and α-particle spectra. Moreover, in many cases a high degree of deformation is necessary to obtain reasonable results.

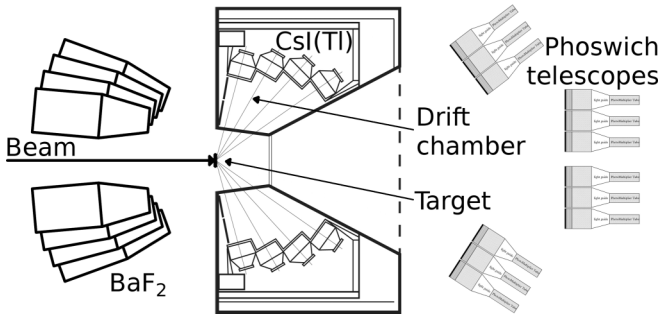

FIG. 1. Lateral view of the composite apparatus used in the experiment.

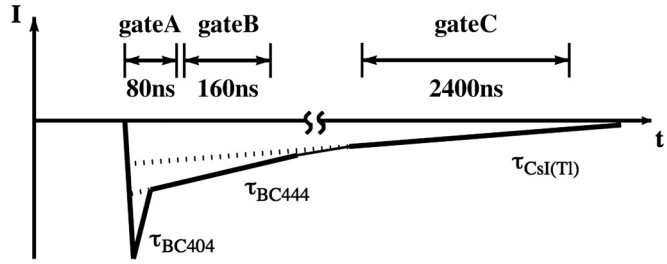

FIG. 2. Sketch of the PMT current signal and of the time windows (not to scale) chosen to obtain the variables gate A, gate B, and gate C of phoswich detectors.

II. EXPERIMENTAL SETUP AND ION IDENTIFICATION

^{88}Mo compound nuclei have been produced at three different excitation energies (1.4, 2.2 and 3.0 MeV/nucleon) by means of fusion reactions performed at the INFN *Laboratori Nazionali di Legnaro* (LNL, Italy). Pulsed beams of ^{48}Ti at the three bombarding energies (300, 450 and 600 MeV) impinged on a metallic ^{40}Ca target (500 μg/cm^2 thickness) sandwiched between two very thin C foils (15 μg/cm^2) to prevent prompt oxidation. Typical beam currents of 0.5–1 p nA were used. In order to study the GDR evolution with excitation energy and spin in molybdenum nuclei, a composite apparatus was used (Fig. 1). A group of eight BaF2 scintillators (Hector setup [10,21,22]) for γ rays, covering backward laboratory angles, was coupled with a large acceptance detector for charged reaction products. Here we describe only this latter part of the setup, while details on the γ array can be found in [10,11].

The heavy products, in particular evaporation residues from the fusion reactions, were detected by an array of 48 triple phoswiches of the Fiasco setup [23] mounted in six matrices, each with eight detectors, in an axially symmetric configuration around the beam direction. The phoswiches featured two plastic layers (made of a fast 180 μm and a slower 5 mm scintillator) followed by a CsI(Tl) crystal 4 cm thick, thus presenting a wide dynamic range for pulse shape analysis. With respect to their original use, these detectors were now equipped with digital electronics [24], purposely developed by the collaboration. The anode current pulses from the photomultipliers were digitized and the relevant information (time mark, pulse shape, and energy-related variables) was extracted. In practice, for each phoswich one obtains, besides a time mark for the time of flight (ToF), three energy-related variables (henceforth gate A, gate B, and gate C) obtained by integration of the current signal inside three different time windows, as schematically shown in Fig. 2; gate C (0.96–3.36 μs) corresponds to the light emitted by the CsI(Tl) with the longest time constant; gate B (96–256 ns) includes the light of the second plastic layer and part of the light emitted by the CsI(Tl); gate A (0–80 ns) includes the fastest light components from all the three scintillator layers.

The phoswiches covered the polar region from around 5° to 25°; 32 of them were located in a wall configuration from 5° to 13° with a significant efficiency for ER detection while the remaining 16 scintillators were placed in two side arms, mainly to detect fission fragments. Thanks to the first fast plastic layer and to the large distance from the target (1.6 m), the phoswiches permitted velocity measurement of the ejectiles from $Z = 1$ up to the ER with good time resolution (of the order of ns). The charge identification, only possible for the products punching through the first thin layer, has been obtained via digital pulse shape methods from protons to Z close to the beam atomic number. The upper limit in charge depends on the particular telescope and on the beam energy, and it never exceeds $Z = 18$. Hydrogen isotopes have been identified also by means of the fast-slow technique in CsI(Tl). Heavy fusion residues and heavy fission fragments, stopped in the first plastic layer, were detected without charge identification. It has to be noted that the time mark given by the phoswich telescopes by means of the digital technique (based on the numerical implementation of the constant fraction discrimination method, used for the first time during this experiment) is progressively delayed when the kinetic energy of the particles increases and thus the energy deposited in the slow plastic layer and in CsI(Tl) grows. This systematic distortion (walk in the time mark detection) was associated with a too small amount of digitized samples which were recorded for each phoswich signal and could not be corrected in the offline analysis. As a consequence, in the following, we discuss velocity spectra for heavy fragments which are stopped in the first layer, while for light products, entering also in the successive layers of the telescopes, we are able to rely only on the particle multiplicities; in fact we judge the velocity (and thus the energy) not trustworthy.

The forward chamber of Garfield [25], covering polar angles between 29.5° and 83° is able to detect light charged particles (LCPs) and intermediate mass fragments (IMFs). Garfield is based on ΔE(gas)-E(CsI(Tl)) modules, equipped with digital electronics, and its features and performances are extensively described elsewhere [25]. Very briefly, Garfield consists of 192 ΔE(gas)-E(CsI(Tl)) telescopes. The gas volume is unique for all the modules and it is filled with flowing CF4 at a pressure around 50 mbar. The collecting anodes of the ΔE stage, based on metal/glass microstrip technology, provide a moderate electron multiplication. While preserving the linear response with deposited energy, the internal gain allows for detection and identification from light charged particles to intermediate mass fragments (typically $Z \approx 10$–12). The 192 ΔE(gas)-E(CsI(Tl)) telescopes are organized in four polar rings corresponding to four CsI(Tl) shapes; each ring consists

of 48 effective sectors, with an azimuthal granularity of 7.5°. In this experiment the mechanical constraints, related to the coupling of the BaF_2 with Garfield, imposed a change in the target holder. As a result the backward ring of Garfield (from 67° to 83°) was affected by the target shadowing and has been discarded in the present analysis.

As already said, for each telescope the ΔE-E method allows identification of charged particles from $Z = 2$ to $Z \approx$ 10–12, measuring also their energy. Moreover, light charged particles ($Z = 1,2$) were isotopically resolved via pulse shape analysis in the CsI(Tl) crystals [26]. The energy calibration of CsI(Tl) has been carried out by exploiting the many reference points collected in various measurements of elastic scattering with low energy beams. The overall uncertainty on the energy measured by the CsI(Tl) is ≈3% to 4%. For kinematic reasons, heavy residues cannot reach the angles of the Garfield setup; as a consequence, Garfield was able to identify (and measure the energy of) all the charged products hitting its active surface.

Finally, a small plastic scintillator was located at $\vartheta \approx 2°$, well below the laboratory grazing angle for all the investigated reactions (the most forward one is $\vartheta_{\rm graz} = 6.9°$ for the 600 MeV reaction). It covered a small solid angle (3.6×10^{-5} sr) and has been used to count elastically scattered ions for absolute cross section normalization.

III. EXPERIMENTAL RESULTS

As stated in the introduction, the topic of this work consists of the investigation of the decay of the excited compound nucleus formed in the ^{48}Ti + ^{40}Ca reaction at three beam energies and the comparison with the prediction of the statistical code.

The main reaction parameters for the investigated systems are reported in Table I. In the columns labeled $l^{B_f=0}_{\rm RLDM}$ and $l^{B_f=0}_{\rm Sierk}$ two estimations of the maximum angular momentum for the existence of the compound nucleus are reported. The former is calculated in the framework of the rotating liquid drop model (RLDM) of [28], while the latter is obtained according to the modified rotating liquid drop model of Sierk [29]. At 300 MeV, where the grazing angular momentum $l_{\rm graz}$ (obtained from [27]) does not exceed by a large amount $l^{B_f=0}_{\rm Sierk/RLDM}$, the complete fusion represents the dominant reaction channel. The formed compound nucleus has a broad spin distribution [11] and it decays either by evaporation [fusion-evaporation (FE) process] or by fission [fusion-fission (FF) process, possibly followed by the evaporative decay from the fission fragments]. The two fission products can be of similar mass (symmetric fission) or may be formed by a lighter and a heavier fragment (asymmetric fission). The FF channel becomes more and more significant with respect to the FE process when the angular momentum of the compound nucleus increases, up to the $l^{B_f=0}_{\rm Sierk/RLDM}$ value, beyond which the system becomes unstable against fission, because the fission barrier vanishes. Beyond $l^{B_f=0}_{\rm Sierk/RLDM}$ fusion is prevented and other reaction mechanisms take place; in particular the deep inelastic process is the most important, but also the quasifusion/quasifission mode (in which the system does not go through a completely equilibrated fused phase) can be present. Those mechanisms, which are supposed to increase with beam energy, produce two heavy residues in the exit channel (for the deep inelastic process, the quasiprojectile QP and the quasitarget QT), similar to symmetric fission. The contribution of such binary channels represents a background for the true FF events which can be barely disentangled, because the populated phase space regions are partly overlapping. These mechanisms affect mainly the symmetric fission case because the two reaction partners are quite similar in terms of mass.

TABLE I. Main reaction parameters. E_b is the beam energy; $E_{\rm c.m.}$ is the available energy in the center of mass, after removing the energy lost in half target; $\vartheta_{\rm graz}$ and $l_{\rm graz}$ are, respectively, the grazing angle and the grazing angular momentum, calculated according to [27]; $l^{B_f=0}_{\rm RLDM}$ is the critical angular momentum beyond which the fission barrier vanishes, calculated according to [28]; $l^{B_f=0}_{\rm Sierk}$ is the critical angular momentum beyond which the fission barrier vanishes, calculated according to [29]; $E^*_{\rm CN}$ is the excitation energy of the compound nucleus, calculated according to the formula $E^*_{\rm CN} = E_{\rm c.m.} + Q$, where Q is the Q value for fusion; $E^*_{\rm CN}/A$ is the excitation energy per nucleon of the compound nucleus; σ_R is the reaction cross section calculated according to [27].

E_b (MeV)	$E_{\rm c.m.}$ (MeV)	$\vartheta_{\rm graz}$ (deg)	$l_{\rm graz}$ ($\hbar$)	$l^{B_f=0}_{\rm RLDM}$ ($\hbar$)	$l^{B_f=0}_{\rm Sierk}$ ($\hbar$)	$E^*_{\rm CN}$ (MeV)	$E^*_{\rm CN}/A$ $\left(\frac{\rm MeV}{\rm nucleon}\right)$	σ_R [mbarn]
300	134.7	15.8	91	79	64	123.8	1.4	1863
450	203.0	9.5	124	79	64	192.4	2.2	2268
600	271.0	6.9	149	79	64	260.7	3.0	2446

A. Selection of fusion events

In order to properly select FE and FF events, a first presorting was done at the trigger level. Indeed, the main trigger was the coincidence of a hit in a phoswich and a hit in Garfield. Considering the phoswich and Garfield acceptances, this condition strongly selects FE events. In order to better suppress undesired events (i.e., elastic scattering and binary peripheral reactions) only detector signals above the noise level but below a given threshold (corresponding to gate A values around 2000 channels; the thick horizontal line in Fig. 3) were allowed to start the data acquisition.

In Fig. 3(a) we show a typical gate A vs ToF correlation, which is the main criterion for the off-line event selection, while in part (b) of the picture the gate A vs gate B correlation is presented. The plots refer to the reaction at 600 MeV. In the gate A vs ToF correlation three different regions can be identified: ions stopped in the first thin plastic scintillator layer (hyperbolic branch at ToF > 40 ns), for which the charge identification is not possible; IMFs and LCPs stopped in the second scintillator layer (spots at different gate A values), for which the charge identification is possible; and finally LCPs (only protons for the reactions at 300 MeV) entering the CsI(Tl) layer (sudden increase of the gate A value). Ions stopped in the first scintillator layer produce the almost vertical and unresolved branch in the gate A vs gate B correlation, while those punching through the fast plastic collapse on the almost horizontal lines, corresponding to the various Z, visible in the

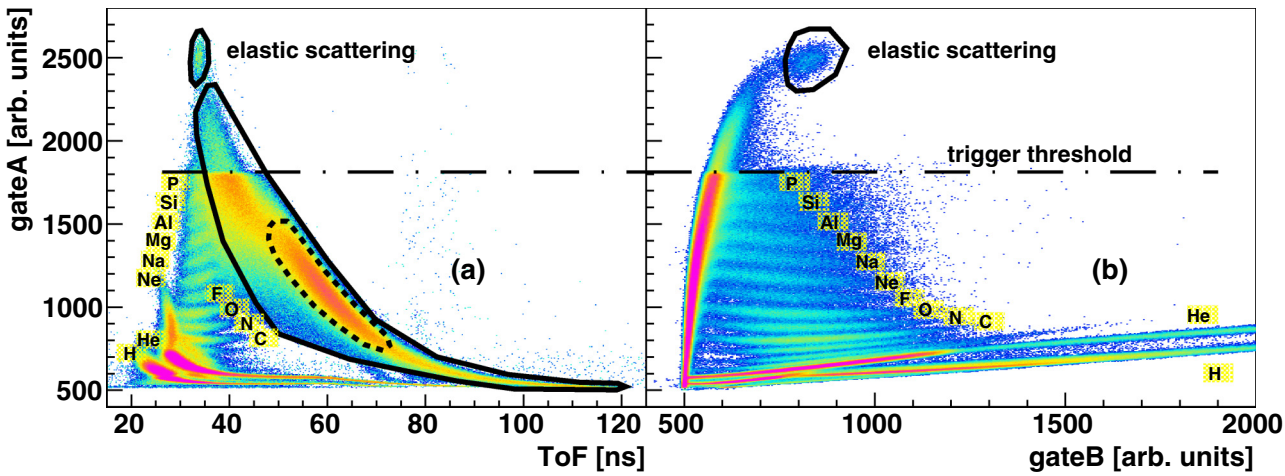

FIG. 3. (a) Correlation between gate A (see text) and the time of flight for a phoswich telescope at $\vartheta \simeq 8.3^\circ$. (b) Correlation between gate A and gate B for the same phoswich telescope. Areal gates for particle identification are shown in the left panel and are explained in the text. Data refer to the reaction at 600 MeV.

picture. LCPs entering the CsI(Tl) give rise to the discontinuity in the lower part of the gate A vs gate B correlation.

FE events are selected by requiring that only one fragment in the phoswich wall be inside the inner dashed-line areal gate drawn on the gate A vs ToF correlation in the region of unresolved heavy products. In the same figure one can clearly see the yield drop above the trigger upper level. The island of events at the highest gate A values corresponds to residual elastic scattered ions and has been used for ToF calibration.

The fission of nuclei with $A \approx 100$, below the Businaro-Gallone point, mainly produces two fragments with different sizes. Therefore we expect that in our system the asymmetric splits prevail, as reported in [30] for molybdenum isotopes.

Candidates for symmetric FF events have been selected requiring the coincidence of two heavy products in the phoswich wall falling inside the outer full-line areal gate drawn on the left side of Fig. 3; instead candidates for asymmetric FF events have been selected by the coincidence of a heavy product in the phoswich wall (inside the same full-line areal gate) and an IMF in whatever detector section. Moreover, candidate fission fragments must have their center-of-mass velocity collinear and their relative velocity compatible with the fission systematics [31,32]. For kinematical reasons, two heavy fragments (symmetric fission) cannot reach Garfield, while only the lighter fragment from asymmetric splits can be detected in Garfield. Whatever the emission angle, the IMF is the only partner of the fission process which can be identified in charge. Of course, asymmetric fission events in which the light partner is missed produce a background of incomplete events for the selected FE event set. This background has been estimated, as described later.

B. Use of the simulation

We first consider the comparison of the experimental observables with GEMINI++ in the reaction at 300 MeV, where the assumption of the formation of the CN following complete fusion is most reliable; in particular, we compared experimental energy spectra and multiplicities of protons and α particles with the prediction of the code for the decay chain of a ^{88}Mo source with the proper excitation energy (1.4 MeV/nucleon) and a triangular spin distribution up to the $l_{\rm crit}$ value. In order to perform a correct comparison, the simulated events were filtered with a software replica of our setup. The main code parameters were tuned in order to obtain the best overall agreement between experimental results and simulated data. In particular, referring to the parameters introduced in [8], we tried to tune the level density parameter $\tilde{a}_{\rm eff}$ (acting, in particular, on the parameter k_0 of Eq. (15) of reference [8]), the spread of the LCP Coulomb barrier taken into account by a parameter w in the transmission coefficients, the yrast parametrization $E_{\rm Y}$, the time delay for fission $\tau_{\rm d}$, and the parametrization of the fission barrier $B_{\rm f}$ as a function of the total angular momentum J. According to [8], the level density parameter rules the slope of the exponential tail of the energy spectra while w controls their shape close to the Coulomb barrier. $E_{\rm Y}$ is particularly significant for light nuclei with small moment of inertia; it affects the emission of α particles which remove large amount of spin and has slight influence on protons. The $\tau_{\rm d}$ parameter and the shape of $B_{\rm f}$ can influence the occurrence of the fission process and its competition with particle decay. The model parameters have been tuned mainly looking at LCP spectra for FE events.

Once a reasonable parameter set has been fixed, we can use simulated events to reliably evaluate the detector efficiency and thus estimate the 4π-corrected particle multiplicities and the absolute cross sections at all the measured beam energies.

C. Fusion-evaporation and fusion-fission events

According to the GEMINI++ simulation, the detection efficiency for the evaporation residues (ER) in FE events has been evaluated to be within 10% and 13% (increasing with the beam energy) with the parametrization giving the best agreement between experimental and simulated LCP spectra (see in the following). In Fig. 4(a) the experimental laboratory velocity distribution for the ER (full symbols) is compared with the simulated one (filtered with a software replica of our setup,

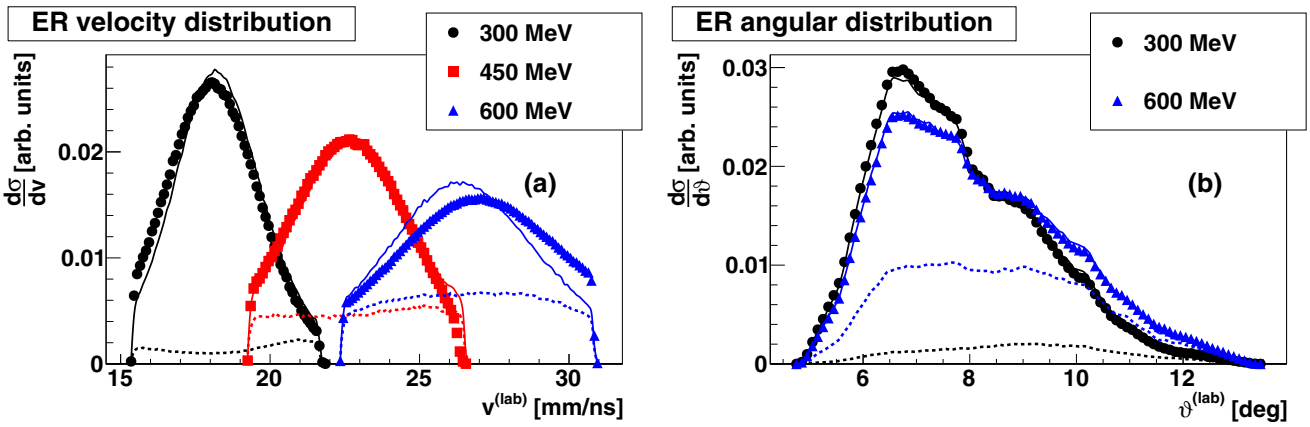

FIG. 4. (a) ER laboratory velocity distribution at the three bombarding energies (black: 300 MeV; red: 450 MeV; blue: 600 MeV); symbols are the experimental data, while continuous lines correspond to GEMINI++ simulation with RLDM yrast, RLDM fission barrier, $w = 1.0$ fm, $\tau_d = 0$ zs (see text). (b) ER laboratory angular distribution at 300 MeV (black) and 600 MeV (blue); symbols are experimental data, while continuous lines correspond to GEMINI++ simulation. In both pictures dotted lines correspond to simulated fission events in which the light partner was lost and the heavy one was erroneously identified as FE. All spectra are normalized to their integral, except for dotted lines (for which the same scaling factor of continuous curves has been used).

continuous lines) for the three different beam energies; spectra are normalized to their integral. Simulated and experimental data are generally well matched, with the partial exception of the 600 MeV case; as a consequence, we can argue that a residual pollution of other reaction mechanisms (not included in the simulation) is present for the highest beam energy. On part (b) of the same figure the experimental laboratory angular distribution of the ER (full symbols) for the reactions at 300 MeV and 600 MeV compared with the GEMINI++ simulation (continuous lines) is plotted. A very good agreement is obtained for this observable. In both sides of Fig. 4 dotted lines correspond to a fission background of ER events where one of the fission products (the lighter one) was lost and the other one fell inside the ER detection gate (dashed contour in Fig. 3). In this case the scaling factor is the same used for the continuous curves. These events show an almost flat angular distribution and they constitute a background of incompletely detected events, present both in simulated and experimental data. According to the GEMINI++ calculation, their amount is about 9% of ER events at 300 MeV, it rises to about 34% of ER at 450 MeV and it is about 50% of the total ER at the highest beam energy.

Protons and α particles represent the dominant contribution in the decay chain of ER in FE events. The experimental center-of-mass energy spectra of protons and α particles at all the investigated beam energies are presented in parts (a) and (b) of Fig. 5, respectively; the spectra are normalized to the number of ER and refer to particles detected in the Garfield ring covering the polar angle between 41° and 52°.

As expected for the decay of a hot nuclear source, the spectra have Maxwellian shape, with the apparent temperature (given by the inverse slope of the high energy tail) increasing with the beam energy, as the excitation energy of the CN increases.

A comparison of the experimental center-of-mass kinetic energy spectra for light particles (black squares) with the

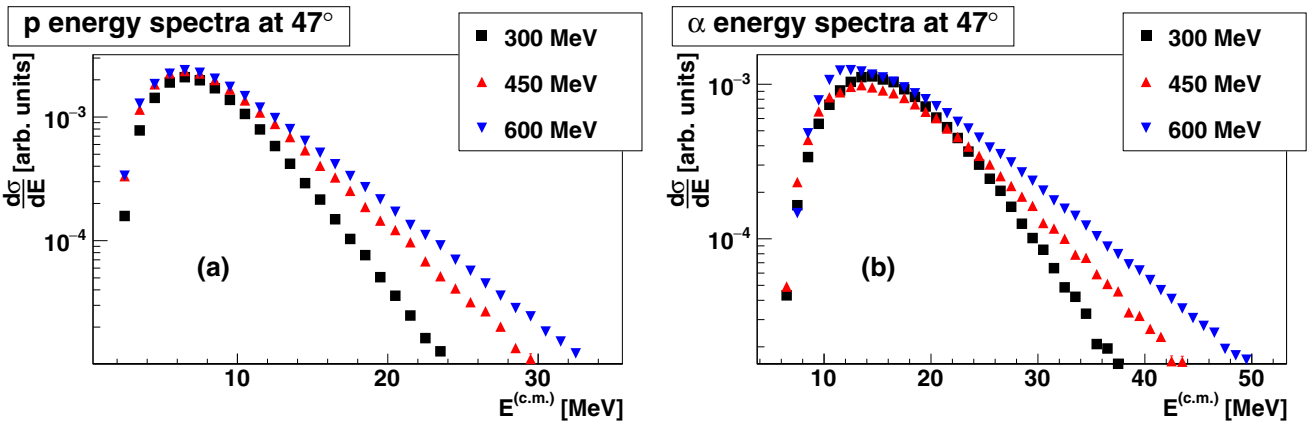

FIG. 5. (a) Experimental center-of-mass energy spectra for protons in the reaction at 300 MeV (black squares), at 450 MeV (red up triangles), and at 600 MeV (blue down triangles), detected in the Garfield ring with polar angles ranging from 41° to 52°. The spectra are normalized to the number of evaporation residues. (b) The same for α particles.

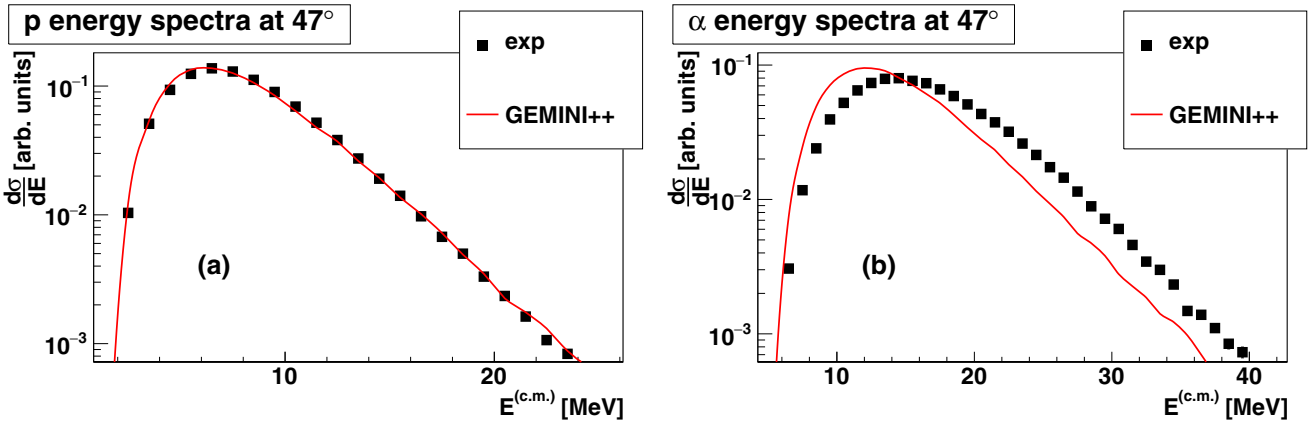

FIG. 6. (a) Center-of-mass energy spectra of protons in the reaction at 300 MeV for experimental data (black squares) and GEMINI++ simulation (red curve) with standard parameters (from [8]). The spectra are normalized to their integrals. Data refer to particles detected in the Garfield ring covering the polar angles between 41° and 52°. (b) The same for α particles.

prediction of the GEMINI++ code (red curve), run with standard values of the parameters (those reported in [8]) and filtered with a software replica of the setup, is plotted in Fig. 6 for the reaction at 300 MeV for particles detected in the Garfield ring covering the polar angle between 41° and 52°. Side (a) concerns protons, while on side (b) α-particle spectra are presented. The spectra are normalized to their integrals, in order to put into evidence differences in their shapes.

From these plots a good agreement emerges between the model and experimental data in the case of protons, while the α-particle spectra are strongly different: in fact the experimental Coulomb barrier is higher than the simulated one.

In order to improve the model agreement in the case of α particles, we investigated the effect of some model parameters, chosen among those mainly influencing the shape of the kinetic energy spectra of evaporated particles as reported in [8].

The effect of the level density parameter was investigated, varying k_0 in the range 6–10 MeV. According to [8] the standard k_0 value for ^{88}Mo CN is 7.3 MeV. Note that, according to Eq. (15) of [8], since the κ parameter is close to 0.1 for $A = 88$, for our system the effective level density parameter $\tilde{a}$ is almost independent of the excitation energy and approximately equal to $\tilde{a} = \frac{A}{k_0}$ [11]. We found that for protons the standard value k_0 of [8] is fine, while no appreciable improvement of the agreement between simulated and experimental spectra could be obtained for α particles in the investigated range. As a consequence, the standard value was kept.

In GEMINI++ the effect of the source deformation due to thermally induced shape fluctuations is taken into account by averaging the transmission coefficients over three different values calculated with three different radius parameters of the nuclear potential (R_0, $R_0 - \delta r$, and $R_0 + \delta r$, Eq. (9) of reference [8]), where $\delta r = w\sqrt{T}$ and T is the nuclear temperature of the daughter nucleus. The spread of the transmission coefficient mainly influences the shape of LCP energy spectra in the Coulomb barrier region and its effect is evident for α spectra, while it is almost negligible for protons, due to their lower Coulomb barrier. The standard GEMINI++ prescription is $w = 1.0$ fm; however, in [8] a case (^{106}Cd, [15]) is presented where $w = 0$ fm (corresponding to a single barrier, i.e., a spherical nucleus) fits better. Note that the author of [8] does not exclude that this discrepancy is due to a possible contamination from reaction mechanisms different from FE. In any case, on the basis of this evidence, we investigated the effect of w on the simulated spectra in the range $w = 0.0$ to 1.5 fm. Proton spectra are not affected by the variation of this parameter, while for α particles a slight improvement (consisting in a shift of the barrier towards the experimental value) has been obtained by decreasing the w parameter.

The other parameter able to influence the shape of energy spectra mainly for α particles and mainly for light systems ($A < 150$) is the shape of the yrast line; in [8] a shape that follows the Sierk parametrization [29] up to a threshold angular momentum and then increases linearly is proposed for light systems (as our ^{88}Mo), obtaining very good agreement with many experimental spectra. However, it has to be noted that the explored spin range in [8] (up to 40–50 $\hbar$) is below the angular momenta reachable by our system (see Table I) and thus this recipe may not work properly in our case. Another shape of the yrast line is delivered by the RLDM of [28].

The two different yrast recipes ([8] and RLDM [28]) for our system are shown in Fig. 7 as solid curves. The two curves are very similar up to $J \sim 35\hbar$; above this value the RLDM yrast (red thick curve) tends to be similar to that of a spherical nucleus (not shown). In the same Fig. 7 we compare also two recipes for the fission barrier, the Sierk prescription [29] (black thin dotted curve) and the RLDM [28] (red thick dotted curve). At a fixed angular momentum the RLDM barrier is higher than the Sierk one, thus reducing the fission probability for the ER. This has influence not only on the shape of the particle energy spectra but also on their multiplicities.

Proton spectra are almost independent of the adopted parametrization, while for α particles the best results are obtained when the RLDM barrier is coupled to the RLDM yrast, as shown in Fig. 8 (blue thick dash-dotted curve). We mention that this particular GEMINI++ parameter set corresponds to the choice made in [11].

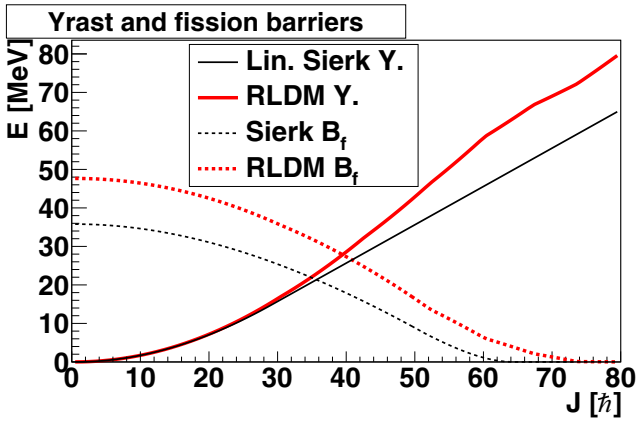

FIG. 7. Solid curves: yrast line parametrizations for ^{88}Mo nuclei as a function of their angular momentum. Black thin curve: linearized Sierk yrast (prescription of [8]). Red thick curve: rotating liquid drop model yrast [28]. Dotted curves: fission barrier parametrizations for ^{88}Mo nuclei as a function of their angular momentum. Black thin curve: Sierk fission barrier [29]. Red thick curve: RLDM fission barrier [28].

The agreement for the energy spectra of α particles can be further improved if we couple the RLDM barrier and RLDM yrast prescription with the choice of $w = 0$ fm, i.e., if we switch off thermal barrier fluctuations, moving towards a spherical nucleus, as it is shown in Fig. 9, blue curve; in particular, the better agreement obtained in the barrier zone (zoomed in the inset) has to be noted.

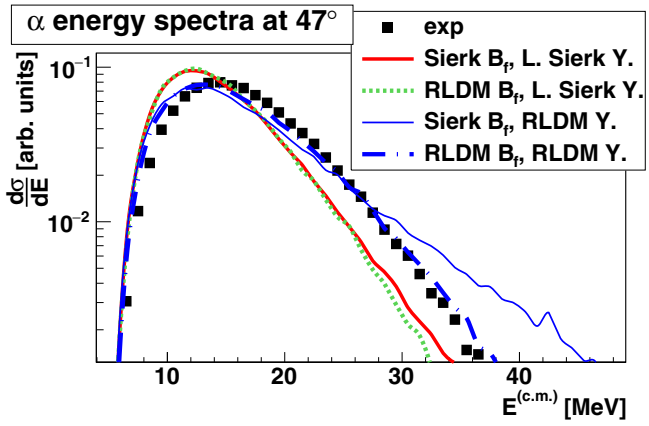

FIG. 8. Center-of-mass energy spectra of α particles in the reaction at 300 MeV for experimental data (black squares) and GEMINI++ simulations with different prescriptions for the fission barrier and the yrast curve. The standard value (Sierk fission barrier and Linearized Sierk yrast) is the red continuous thick curve; the green dotted curve corresponds to standard yrast (linearized Sierk yrast) and RLDM fission barrier; the thin blue curve corresponds to standard fission barrier (Sierk fission barrier) and RLDM yrast; the blue dash-dotted curve corresponds to RLDM fission barrier and RLDM yrast. Spectra are normalized to their integrals. Data refer to particles detected in the Garfield ring covering the polar angles between 41° and 52°.

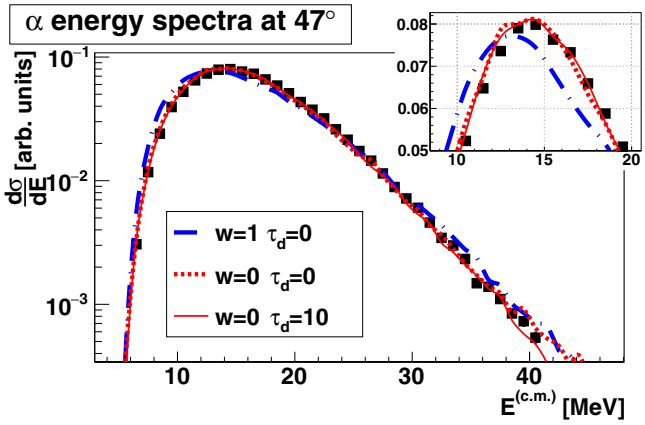

FIG. 9. Center-of-mass energy spectra of α particles in the reaction at 300 MeV for experimental data (black squares) and GEMINI++ simulations with different prescriptions. Blue curve: RLDM fission barrier, RLDM yrast line, $w = 1.0$ fm, and $\tau_d = 0$ zs. Red curve: RLDM fission barrier, RLDM yrast line, $w = 0$ fm, and $\tau_d = 0$ zs. Red dotted curve: RLDM fission barrier, RLDM yrast line, $w = 0$ fm, and $\tau_d = 10$ zs. In the inset the barrier region is zoomed with a linear ordinate scale. Spectra are normalized to their integrals. Data refer to particles detected in the Garfield ring covering the polar angles between 41° and 52°.

The time delay for fission τ_d has no influence on the particle energy spectra (Fig. 9, comparison between red continuous and red dotted curves), while it affects the fission probability and the angular distribution of the emitted particles (as will be discussed in relation to Fig. 13).

The experimental center-of-mass energy spectra of protons [panels (a), (b), (c)] and α particles [panels (d), (e), (f)] for three angular rings of Garfield are compared in Fig. 10 with the corresponding simulated distributions obtained with the "best" set of parameters so far discussed ($k_0 = 7.3$ MeV, RLDM fission barrier, RLDM yrast line, $w = 0$ fm, $\tau_d = 10$ zs). The agreement between experimental data and simulation is reasonable at all angles accessible with Garfield.

Calculations have been extended to the two higher beam energies assuming the parameter set tuned for the 300 MeV reaction.

The center-of-mass energy spectra of protons [panels (a), (b), (c)] and α particles [panels (d), (e), (f)] for the reactions at 450 and 600 MeV are displayed in Figs. 11 and 12, respectively. Also in this case a reasonable agreement at all the explored laboratory angles is observed between simulated and experimental data.

Laboratory angular distributions for protons [panels (a), (b), (c)] and α-particles [panels (d), (e), (f)], normalized to the number of ER, are shown in Fig. 13 for all the investigated reactions [panels (a) and (d): 300 MeV; (b) and (e): 450 MeV; (c) and (f): 600 MeV]. Experimental data are plotted as black full circles, while different GEMINI++ calculations, all assuming RLDM yrast line and RLDM fission barrier, correspond to different colors. The horizontal bar in the Garfield region ($\vartheta > 30°$) indicates the angular coverage of each ring. The vertical error bars for experimental data represent estimated systematic errors due to the evaluation of the efficiency in the

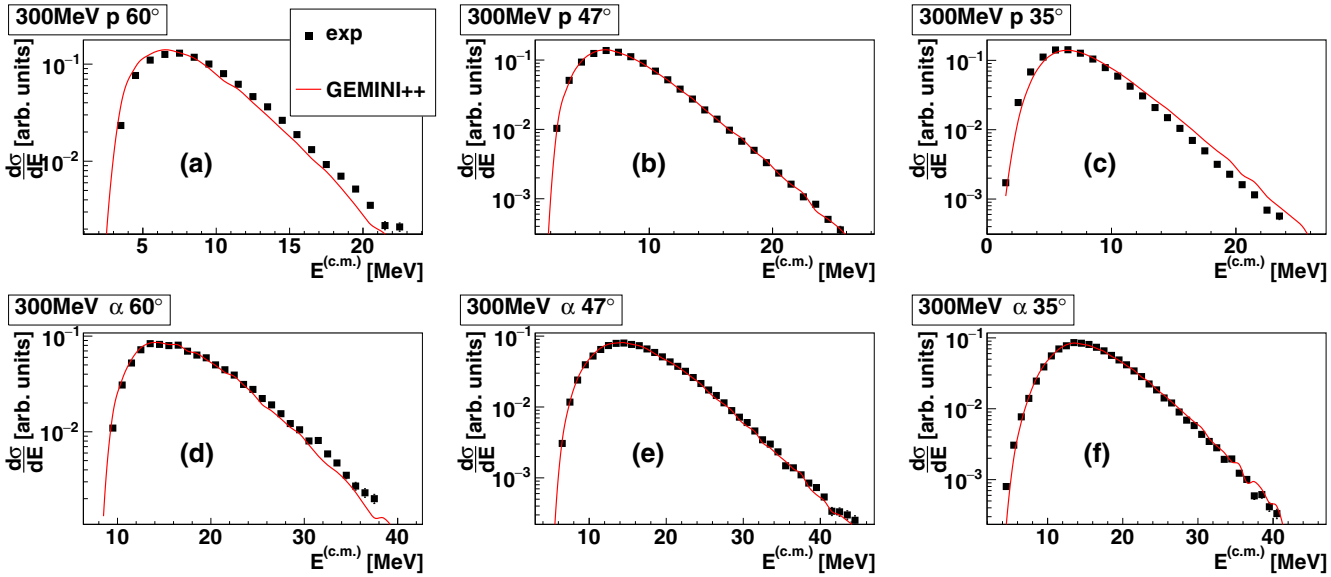

FIG. 10. Center-of-mass energy spectra for LCPs detected at different laboratory angles for the reaction at 300 MeV. Experimental data correspond to black squares. Simulated data have been obtained with $k_0 = 7.3$ MeV, RLDM fission barrier, RLDM yrast line, $w = 0$ fm, $\tau_d = 10$ zs. Spectra are normalized to their integral. (a) and (d): $53.0^\circ \leqslant \vartheta_{\rm lab} \leqslant 66.0^\circ$; (b) and (e): $41.0^\circ \leqslant \vartheta_{\rm lab} \leqslant 52.0^\circ$; (c) and (f): $29.5^\circ \leqslant \vartheta_{\rm lab} \leqslant 40.0^\circ$. Panels (a), (b), (c) correspond to protons, while panels (d), (e), (f) correspond to α -particles.

individual detection cells; statistical errors are negligible. The main observations are as follows. Concerning proton emission, the data are overall well described by the statistical model at the three energies, whatever the input parameter choice. There are minor discrepancies which are different for the three bombarding energies; at 300 MeV the model underestimates the proton yields beyond 30°, while the opposite happens at 600 MeV. However, the measured proton emission appears to be essentially compatible with the evaporation from ^{88}Mo compound nuclei. The most striking difference between experiment and model is for α emission, as the measured distribution becomes more forward peaked than the model predictions when the energy increases, almost independently of the fine tuning of the parameters. There are of course some changes if some parameters are modified. For example, the best set from the point of view of the shape of the energy spectra ($w = 0$ fm, $\tau_d = 10$ zs, red squares) gives the worst agreement for the forward emission. The choice $w = 1.0$ fm (green up triangles and blue down triangles), corresponding to a slightly poorer reproduction of the α energy spectra (see Fig. 9), increases the forward focusing of α particles, with a minor effect of the delay time for fission ($\tau_d = 0$ zs for blue down triangles, $\tau_d = 10$ zs for green up triangles). In any case, the experimental focusing of α particles, increasing with

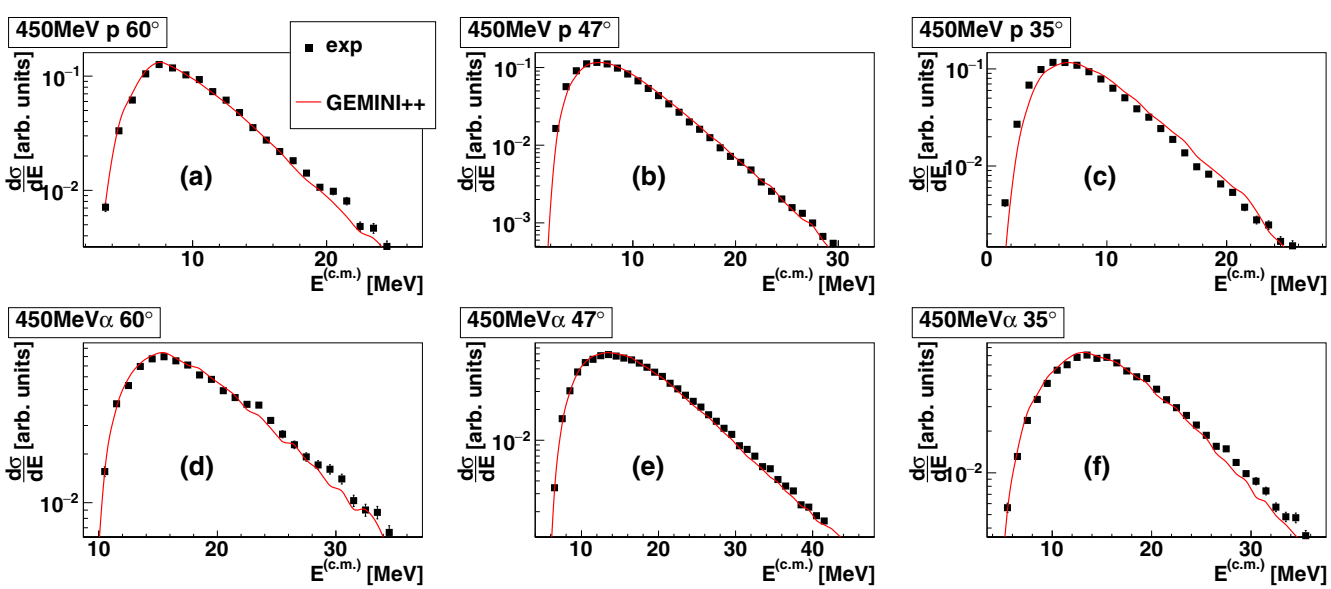

FIG. 11. The same as Fig. 10 but for the reaction at 450 MeV.

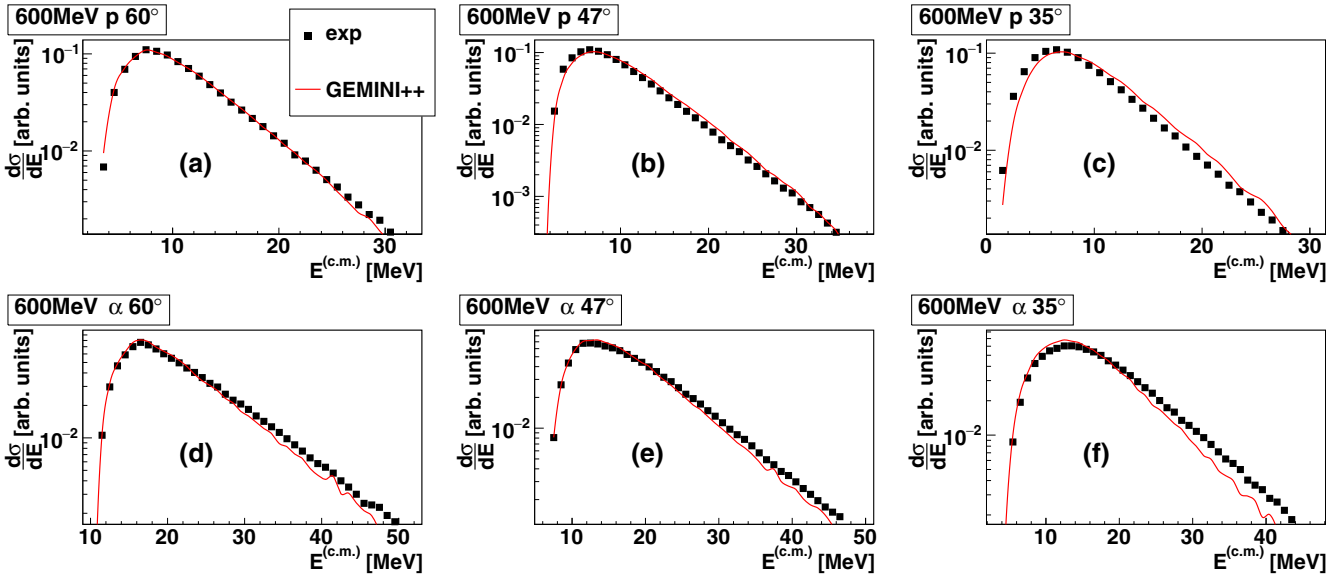

FIG. 12. The same as Fig. 10 but for the reaction at 600 MeV.

the beam energy, cannot be properly reproduced by the model code.

Concerning the origin of the observed yield discrepancy for α particles, we have tested several hypotheses. For example, the possibility that the ^{40}Ca target is oxidized (and, as a consequence, causes a spurious emission of α particles) has been excluded by means of a chemical analysis on the sample. A possible source of α contamination comes from the C layers embedding the ^{40}Ca; the detected events can contain a contribution from the complete fusion of ^{48}Ti and ^{12}C. This hypothesis has been rejected too, because of the very different center-of-mass velocity of the $^{48}\mathrm{Ti} + {}^{12}\mathrm{C}$ system with respect to ^{88}Mo (they differ by about 12 mm/ns at 600 MeV and about 9 mm/ns at 300 MeV): events coming from the complete fusion of ^{48}Ti and ^{12}C are well outside the selected ER gate (Fig. 3). The fission background of ER events (not negligible, mainly at 600 MeV) is already included in the GEMINI++ simulation; any attempt to reduce this spurious contribution by means of a strict cut on the most forward emitted ER has little effect since GEMINI++ shows that the angular distribution of the background fission fragment is rather broad and flat. In any case, as shown by Fig. 14 for

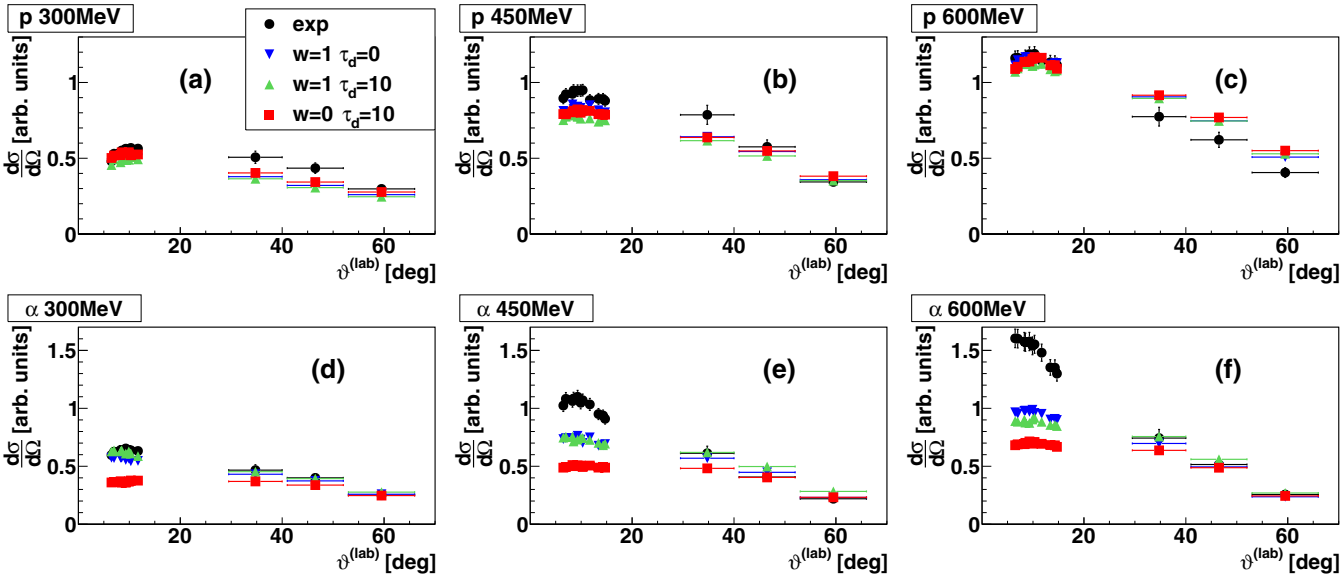

FIG. 13. Differential cross section as a function of the laboratory polar angle. Panels (a), (b), (c): protons. Panels (d), (e), (f): α particles. (a) and (d): 300 MeV; (b) and (e): 450 MeV; (c) and (f): 600 MeV. Full black circles: experimental data. Red squares: GEMINI++ with RLDM yrast line, RLDM fission barrier, $w = 0$ fm, $\tau_d = 10$ zs (best choice for energy spectra). Blue down triangles: GEMINI++ with RLDM yrast line, RLDM fission barrier, $w = 1.0$ fm, $\tau_d = 0$ zs. Green up triangles: GEMINI++ with RLDM yrast line, RLDM fission barrier, $w = 1.0$ fm, $\tau_d = 10$ zs.

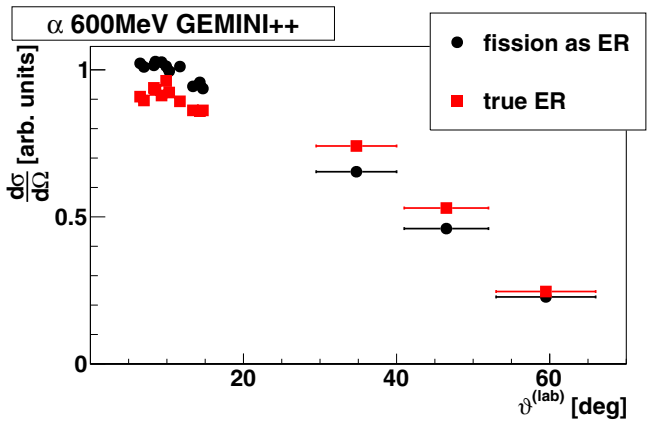

FIG. 14. Simulated angular distribution for α particles at 600 MeV; GEMINI++ data with RLDM yrast line, RLDM fission barrier, $w = 1.0$ fm, and $\tau_d = 0$ zs. Red squares correspond to events in which a true ER is selected, while black dots correspond to incomplete events in which a fission fragment produces a background of the fusion channel.

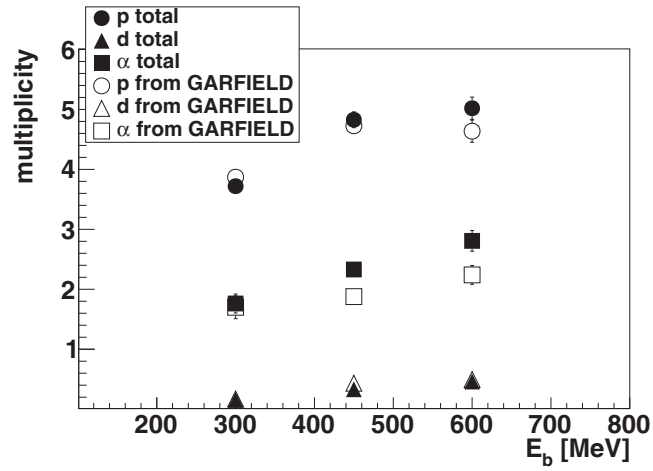

FIG. 15. Estimated experimental particle multiplicities in 4π as a function of the beam energy in FE events. Circles: protons; triangles: deuterons; squares: α particles. Full symbols refer to data from Garfield and phoswich detectors. Open symbols give the particle multiplicities extracted from Garfield data only.

α particles at 600 MeV, we have verified that, according to GEMINI++, particles emitted by a fission fragment erroneously identified as ER are only weakly more forward focused (full black dots) with respect to the case of true ER (red squares); as a consequence, they cannot explain the observed discrepancy between simulation and experimental data.

Concerning deep inelastic collisions, not included in the adopted model, we note that for kinematical reasons only a small tail of QP/QT from very dissipative collisions could fall inside in the ER identification gate. As a consequence the possible contamination should be negligible, although a simulation of the DIC process based on a phenomenological parametrization of this mechanism indicates a preferential emission of α particles in the forward direction at 600 MeV. Other processes such as quasifusion/quasifission are not included in the model and could contaminate in a minor way the experimental sample of ER events.

With the above limitations, we can use GEMINI++ data in order to estimate the efficiency for LCP detection and to correct the measured yields. Various slightly different correction factors have been deduced according to the different adopted parametrizations of GEMINI++. The resulting LCPs' 4π multiplicities obtained by averaging over the values obtained with different parameter sets are reported in Fig. 15 for protons, α particles, and deuterons, exploiting the isotopic resolution for hydrogen isotopes both for Garfield and the phoswich telescopes; tritons are too weak to be reliably evaluated.

Vertical error bars correspond to the standard deviation of the different results. A statistical error of the order of 8% for protons (circles), 20% for deuterons (triangles) and 10% for α particles (squares) is also associated with each point. The plot shows that particle multiplicities slightly increase with the beam energy, with a weaker trend for protons. The observed forward focusing of α particles increasing with bombarding energy suggests the onset of pre-equilibrium processes. Therefore, we tried to estimate α multiplicities separately from Garfield data only (extrapolating them to the full solid angle), where angular distributions and yields are quite well reproduced by the statistical model. The same choice can be applied also to protons, although no clear evidence of a model failure with increasing energy exists (Fig. 13 top part). The obtained results are shown as open symbols in the same Fig. 15. For α particles the difference between the two data sets represents an upper limit for pre-equilibrium emission that, as expected, increases with the beam energy, or, in any case, for emission sources not included in the simulation. In contrast, for protons there is no significant discrepancy at all energies; even at 600 MeV the two extracted proton multiplicities are compatible within the errors. For α particles the possible pre-equilibrium contribution starts at 450 MeV and corresponds to about 0.5 particles per event (with respect to a total number of 2.8 α particles per event) in the worst case (600 MeV), thus justifying the assumption of negligible pre-equilibrium effects done in [11] for the evaluation of the GDR strength. On a theoretical ground there are some hints from exciton models which assume some α-particle preformation inside nuclei [33–36]; as a consequence it is possible that α particles are favored in pre-equilibrium emission. Moreover, in [37], an experimental analysis of α-particle spectra is discussed and data are interpreted considering the α particle as an exciton and a preformation factor is extracted. Another example is given in [38] where an excess α-particle emission was found in asymmetric-mass dissipative collisions at rather low bombarding energies ($\sim$6 MeV/nucleon).

By means of the fast plastic scintillator located below the grazing angle for all reactions (see Sec. II) it has been possible to estimate absolute cross sections. For FE events, the obtained values are reported in Table II in the row labeled σ_{FE}; they are the average among the various estimated σ_{FE} values obtained running GEMINI++ with different sets of parameters (all of them with RLDM yrast line and RLDM fission barrier). The error is the standard deviation of these values. It is interesting

TABLE II. Experimental absolute cross sections. σ_{FE} is the fusion-evaporation cross section; σ_{FF} is the fusion-fission cross section. σ_F/σ_R is the ratio between the total fusion cross section (FF plus FE) and the total reaction cross section, taken from the last column of Table I. σ_{FE}/σ_R is the ratio between the FE cross section and the total reaction cross section.

	300 MeV	450 MeV	600 MeV
σ_{FE}	(893 ± 109) mb	(545 ± 45) mb	(459 ± 115) mb
σ_{FF}	(115 ± 3) mb	(266 ± 37) mb	(417 ± 114) mb
σ_F/σ_R	0.54 ± 0.06	0.358 ± 0.004	0.36 ± 0.07
σ_{FE}/σ_R	0.48 ± 0.06	0.24 ± 0.02	0.19 ± 0.05

to note that, as shown in the last row of the table, the FE cross section is almost one half of the reaction cross section (last column of Table I) at 300 MeV, while it decreases to about 19% at 600 MeV.

If we plot the normalized FE cross section σ_{FE}/σ_R as a function of the available c.m. energy per nucleon as proposed in the recent systematics for fusion evaporation [9], we can see (Fig. 16) that our data (red dots) fairly agree with the reported prescription.

Finally, we briefly discuss the fission case in order to extract the absolute cross section for this channel. The fission process is mainly associated with the highest angular momenta, as is evident from Fig. 7, dotted lines. In the adopted parametrization (RLDM fission barrier) the barrier is around 50 MeV at low J (as calculated also in [39]) and decreases smoothly, until it vanishes around $79\hbar$. In the experimental data the symmetric fission is weak, the measured fraction varying from 10% to 30% of the total fission events (without geometrical correction), depending on the bombarding energy. The absolute fission cross section σ_{FF} is reported in Table II, second row: its weight in the total fusion cross section smoothly increases from 300 to 600 MeV. At 600 MeV the FF cross section is of the same order of magnitude as the FE cross section. If we compare the total fusion cross section with the total reaction cross section σ_F/σ_R (third line of Table II) we can see that also at 300 MeV there is room for other reaction mechanisms (such as DIC): in fact fusion represents only 54% of the total reaction cross section.

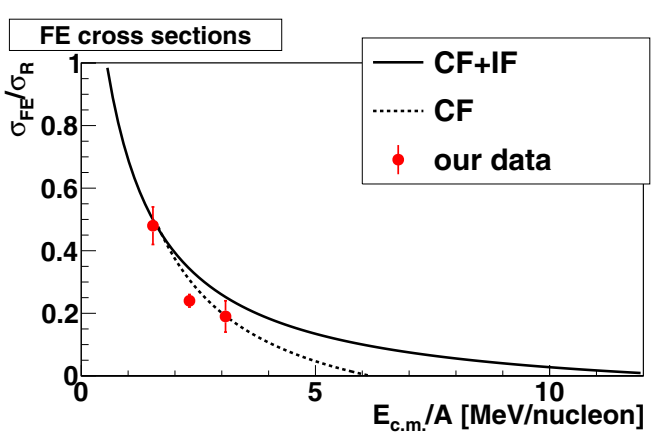

FIG. 16. FE cross section normalized to the reaction cross section as a function of $E_{c.m.}/A$. Red dots correspond to the experimental values found in this work, compared with the systematics of [9] for complete fusion (dotted line) and for the sum of complete and incomplete fusion (continuous line).

IV. SUMMARY AND CONCLUSIONS

In this work we presented some exclusive data concerning the system $^{48}Ti + ^{40}Ca$ at three bombarding energies (300, 450, and 600 MeV). Data have been collected by means of the Garfield setup coupled to a wall of phoswich telescopes of the Fiasco device.

We have focused our analysis on the fusion channel whose collective dipolar excitation has been the subject of our recent investigation [11]. In particular we have shown that this channel represents more than 50% of the total reaction cross section at 300 MeV and it goes down to about 40% at 600 MeV.

As expected, the formed CN decays through the evaporation of LCPs (fusion-evaporation event) or can undergo fission (fusion-fission event). After selecting FE events, we have constrained the main parameters of the statistical code GEMINI++ comparing measured and simulated LCP distributions at 300 MeV where contributions from sources other than the CN should be negligible. We have seen the following:

(1) Proton energy spectra are reproduced by GEMINI++ with the standard parameters.
(2) In the case of α-particles it is necessary to use the RLDM parametrization both for the yrast line and the fission barrier, and to reduce the LCP Coulomb barrier fluctuations. This can indicate rather spherical excited nuclei as the sources of the detected LCP.
(3) At the two highest beam energies there is an excess of α particles at forward angles, which cannot be reproduced by the statistical model.
(4) This excess, corresponding on the whole to about 20% of the total emitted α particles at the highest energy (600 MeV), may be due both to pre-equilibrium emission and to other processes (such as deep inelastic collision, quasifission/quasifusion), whose residual contamination cannot be definitely excluded due to the difficulty of a very clean fusion channel selection.
(5) This excess of α emission can be taken as an upper limit for the pre-equilibrium emission of this system, thus justifying the assumption done in [11] of negligible pre-equilibrium.

Finally we have extracted the absolute cross section for the FE and FF cases:

(1) The FE cross sections are in reasonable agreement with the existing systematics reported in [9];
(2) The total fusion cross section is well below the total reaction cross section (estimated according to [27]), suggesting the presence of other processes, such as DIC, sizably contributing at the highest angular momenta.

ACKNOWLEDGMENTS

The authors thank Prof. P. R. Maurenzig, retired from Dipartimento di Fisica, Università degli Studi di Firenze, Italy, for useful discussions during the data analysis presented in this work. The authors would like to thank also Prof. R. J. Charity from Washington University of St. Louis (Missouri, USA) for support in the use of the GEMINI++ code. This work was possible thanks to the good beam provided by LNL accelerator crew and to the work of the LNL target laboratory staff. This work was supported by the Polish Ministry of Science and Higher Education, Grants No. N N202 486339, No. 2011/03/B/ST2/01894, and No. 2013/08/M/ST2/00591, and by the Polish Science Centre Grant No. 2015/17/B/ST2/01534, and by the French-Polish agreements IN2P3-COPIN (Projects No. 06-126, No. 05-119, No. 09-136, and No. 12-145). This work was also partially supported by grants of Italian Ministry of Education, University and Research under contract PRIN 2010-2011.

[1] P. Roy *et al.*, Phys. Rev. C **86**, 044622 (2012).
[2] L. Morelli *et al.*, J. Phys. G **41**, 075107 (2014).
[3] L. Morelli *et al.*, J. Phys. G **41**, 075108 (2014).
[4] A. Di Nitto *et al.*, EPJ Web Conf. **21**, 02002 (2012).
[5] A. Dey *et al.*, Phys. Rev. C **74**, 044605 (2006).
[6] V. Baran *et al.*, Phys. Rep. **410**, 335 (2005).
[7] A. Ono, Phys. Rev. C **59**, 853 (1999).
[8] R. J. Charity, Phys. Rev. C **82**, 014610 (2010).
[9] P. Eudes *et al.*, Europhys. Lett. **104**, 22001 (2013).
[10] M. Ciemała *et al.*, EPJ Web Conf. **66**, 02020 (2014).
[11] M. Ciemała *et al.*, Phys. Rev. C **91**, 054313 (2015).
[12] S. J. Sanders, Phys. Rev. C **44**, 2676 (1991).
[13] G. La Rana *et al.*, Phys. Rev. C **35**, 373 (1987).
[14] C. M. Brown *et al.*, Phys. Rev. C **60**, 064612 (1999).
[15] G. Nebbia *et al.*, Nucl. Phys. A **578**, 285 (1994).
[16] F. Pühlhofer, Nucl. Phys. A **280**, 267 (1977).
[17] C. Bhattacharya *et al.*, Phys. Rev. C **65**, 014611 (2001).
[18] M. Kildir *et al.*, Phys. Rev. C **46**, 2264 (1992).
[19] M. Brekiesz *et al.*, Nucl. Phys. A **788**, 224 (2007).
[20] M. Kmiecik *et al.*, Acta Phys. Pol. B **38**, 1437 (2007).
[21] A. Giaz *et al.*, Phys. Rev. C **90**, 014609 (2014).
[22] A. Maj *et al.*, Nucl. Phys. A **571**, 185 (1994).
[23] M. Bini *et al.*, Nucl. Instrum. Methods A **515**, 497 (2003).
[24] G. Pasquali *et al.*, Nucl. Instrum. Methods A **570**, 126 (2007).
[25] M. Bruno *et al.*, Eur. Phys. J. A **49**, 128 (2013).
[26] L. Morelli *et al.*, Nucl. Instrum. Methods A **620**, 305 (2007).
[27] S. K. Gupta *et al.*, Z. Phys. A **317**, 75 (1984).
[28] S. Cohen *et al.*, Ann. Phys. (N.Y.) **82**, 557 (1974).
[29] A. J. Sierk, Phys. Rev. C **33**, 2039 (1986).
[30] K. X. Jing *et al.*, Nucl. Phys. A **645**, 203 (1999).
[31] V. E. Viola Jr., Nucl. Data Sheets **1**, 391 (1965).
[32] V. E. Viola, K. Kwiatkowski, and M. Walker, Phys. Rev. C **31**, 1550 (1985).
[33] A. Iwamoto and K. Harada, Phys. Rev. C **26**, 1821 (1982).
[34] S. Kunieda *et al.*, EPJ Web Conf. **21**, 09003 (2012).
[35] P. E. Hodgson and E. Běták, Phys. Rep. **374**, 1 (2003).
[36] O. V. Fotina *et al.*, Int. J. Mod. Phys. E **19**, 1134 (2010).
[37] A. Chevarier *et al.*, Phys. Rev. C **11**, 886 (1975).
[38] H. Ho *et al.*, Z. Phys. A **283**, 235 (1977).
[39] A. Dobrowolski *et al.*, Acta Phys. Pol. B **40**, 705 (2009).